Structure dependence of molecular reactions on surfaces

Cao, K.

Chapter 5

Structure dependence of HD formation on curved Pt(111) surface

5.1 Introduction

For decades, flat single crystals have served as work horse models in fundamental studies of heterogeneous catalysis [91]. Originally, low Miller-index surfaces, e.g. the (111) and (100) surfaces for metals with a face-centered cubic (fcc) unit cell, caught most attention. Vicinal surfaces, e.g. the fcc (221), (533), and (997) surfaces, soon followed as these contain lower coordinated atoms in monoatomic step edges. Such steps mimic the edges on actual catalyst particles. To study the effect of a lowered coordination number of surface atoms to catalytic activity, simple model reactions, e.g. dissociation of molecular H_2 and D_2, and HD formation from these isotopologues were employed [92–99].

Being the simplest overall heterogeneously catalyzed chemical reaction based on more than a single elementary reaction, a kinetic model for HD formation contains the following elementary reactions

$$H_2(g) \rightarrow 2H_{ads} \tag{5.1}$$

$$D_2(g) \rightarrow 2D_{ads} \tag{5.2}$$

$$H_{ads} + D_{ads} \rightarrow HD(g) \tag{5.3}$$

Dissociative adsorption of H_2 and D_2 is followed by recombinative desorption of HD. If there is no isotopic effect to dissociative adsorption and recombinative desorption, the entire mechanisms reduces to

$$A_2(g) \rightleftharpoons 2A_{ads} \tag{5.4}$$

as H and D may both be represented by A. However, as the reactants and products have different molecular masses, mass spectrometry can be used to measure the extent of HD formation, i.e. the extent to which equilibrium is reached. At equilibrium, the ratios of partial pressure, $p_{H_2} : p_{D_2} : p_{HD}$, should be 1:1:2, as formation of HD competes with recombinative formation of H_2 and D_2. Below, we review studies that focused on elementary steps and the overall mechanism for Pt(111)-type surfaces.

The elementary dissociative adsorption of hydrogen, i.e. equations (5.1) and (5.2), was originally studied in greatest detail using supersonic molecular beam techniques for Pt(111) by Luntz et al.[22]. They found evidence of energetic corrugation, i.e. a distribution of barriers to dissociation, with no threshold. Reactivity, as quantified by the incident energy dependence of the initial dissociation probability, $S_0(E_{kin})$, increased smoothly from the lowest attainable incident energy up to 0.55 eV for normal incidence. A study of the polar angle dependence to dissociation showed that normal energy scaling (NES) does not hold, although exchanging normal for parallel momentum reduces reactivity. They reported an absence of isotope effects and an independence of both surface temperature and nozzle temperature, concluding that dissociation is direct and proceeds over a range of barriers. Samson et al.[21] verified the energetic corrugation, finding absolute reactivities that agree with Luntz's data. Recently, we studied this system's polar and azimuthal dependence for D_2 dissociation, as discussed in Chapter 3. Our data also showed nearly perfect quantitative agreement with Luntz's polar angle dependences and absolute dissociation probabilities for a range of incident energies. In agreement with the most recent dynamical calculations for this system[39], we concluded that the system shows, at most, very little geometric corrugation.

Using flash desorption, Lu and Rye already showed in the 1970's that the dissociation probability of molecular hydrogen for four Pt surfaces decreased in the order: (110) > (211) > (100) > (111)[92]. Besides ordering the reactivity of low Miller index surfaces, it clearly showed that corrugation in the form of monoatomic steps aids the

dissociation process. The (211) surface combines a 3-atom wide (111) terrace with A-type steps, i.e. steps made of a monoatomic (100) facet. In Somorjai's notation, this is Pt[3(111)×(100)]. In a similar study, Christmann and Ertl showed two years later that the presence of B-type steps also increased the initial dissociation probability[99]. The (997) surface, consisting of 8-atom wide (111) terraces separated by monoatomic (110) facets, or Pt[8(111)×(110)], was a factor of four more reactive than Pt(111) in dissociating molecular hydrogen. Both studies used dissociation from a bulb gas to create a surface coverage of H_{ads}, Θ_H, at a low surface temperature, T_s. A temperature ramp was started to quantify with temperature programmed desorption (TPD) how much H_2 had dissociated after a particular exposure. Hence, their measure of reactivity toward dissociation averages over a wide range of incident kinetic energies and angles with respect to the surface normal for molecular hydrogen.

Many years later, Gee et al. studied the role of monoatomic A-type steps in the dynamics of hydrogen dissociation using the Pt(533) or Pt[4(111)×(100)] surface and supersonic molecular beam techniques[26]. Whereas S_0 increased similar to Pt(111) at higher incident energies for this surface, it dramatically decreased with increasing kinetic energy up to $\sim$ 150 meV. Their suggestion that step sites allow for new dynamical mechanisms to dissociation was corroborated by dynamical calculations performed in the group of Baerends on the first detailed potential constructed for H_2 and Pt(211)[31, 32]. Using a series of Pt single crystals that contain A-type steps with (111) terraces of various widths, Groot et al. separated the reactivity for molecules impinging onto the A-type step and the (111) terraces [28–30]. They refined a simple mathematical model from Baerends and coworkers and accurately predicted the reactivity of hydrogen dissociation for all Pt[n(111) × (100)] type surfaces based on measurements for Pt(211) alone. The model relies on separation of the dissociation probability into three dynamical components, two of which only occur at the monoatomic steps. As there is no dependence on a molecularly-bound intermediate state that may diffuse from site of impact to some other more reactive site, S_0 scales linearly with step density. We recently showed that the only other model for molecular hydrogen dissociation on Pt(111), i.e. a model relying predominantly on an indirect process to dissociation at step and kink defects via diffusion of a physisorbed molecular intermediate[20, 100], does not correctly predict reactivity

over a large range of step densities [101]. Reactivity also does not follow the expected surface temperature dependence for this model.

For the overall mechanism of HD formation, the isotopically-independent direct dissociation of molecular hydrogen at steps and terrraces sites is followed by recombination of adsorbed atoms and their immediate desorption, i.e. reaction (5.3). Greenlief et al. studied H-D exchange on Pt(111) using temperature programmed desorption (TPD)[102]. They found no isotope effect in desorption after dosing the isotopically pure molecules at a surface temperature, T_s, above 250 K. They reported an activation energy for recombinative desorption of 6.7 ± 0.4 kJ mol^{-1}. Verheij et al. also conducted experiments on Pt(111) investigating HD formation from an H_2 molecular beam with D_2 dissociation from a bulb gas[103]. By detecting HD in an angular resolved fashion and measuring its kinetic energy, they reached the conclusion that two parallel mechanisms for adsorption and desorption were causing HD formation. For stepped surfaces, Somorjai et al. had already studied HD formation using both effusive and supersonic molecular beam techniques in combination with background dosing [93–98]. Originally, the H-D exchange reaction was only detectable on high Miller index Pt single crystal surfaces with B-type steps. Later, they also found it to occur on Pt(111) and concluded that doubling the step density doubles the reaction probability at higher temperatures [95]. Christmann and Ertl showed in their TPD-based study that the presence of B-type steps enhances the activity in H-D exchange between H_2 and D_2 by an order of magnitude for Pt(997) compared to Pt(111)[99].

In this chapter, we introduce the use of a small curved Pt single crystal with its apex oriented to expose the (111) surface and its macroscopic curvature ideally resulting from monoatomic A-type and B-type steps. Such a small curved crystal surface was studied recently by Walter et al. probing both the clean surface and the effect of surface strain on adsorbed CO [104]. We used the combination of supersonic molecular beams and a large Ni cylindrical crystal before to study elementary dissociation[88]. Very recently, we did the same using a small curved Pt single crystal[101]. Here, we show that such a small single crystal also serves to study overall reaction mechanisms through the H-D exchange between H_2 and D_2. However, such crystals must be treated carefully to obtain the ideal structure, consisting of atomically flat terraces and monoatomic steps. Curved single crystal surfaces may locally contain surface structures that are unstable under particular cleaning

or annealing conditions, as shown, for example, by Ilyn et al. for a Ni curved single crystal[105]. Especially since surface reconstruction have been found and studied for flat Pt single crystals exposing the (111) terraces surface, e.g. for Pt(997)[106–108], and such reconstructions may be related to exposure to O_2 and high-temperature annealing, a detailed study of our curved Pt single crystal and cleaning procedures is necessary.

5.2 Experimental methods

All experiments are carried out with a home-build ultra high vacuum (UHV) apparatus 'LIONFISH' (base pressure is below 1×10^{-10} mbar). The UHV system is attached to a double differentially pumped supersonic molecular beam line and contains, a.o., a fixed quadrupole mass spectrometer (QMS, Pfeiffer QMA 200), a quadrupole mass spectrometer (UTI, 100C) that can be moved along the molecular beam axis with an x, y, z manipulator, and LEED/AES optics (OCI BDL800IR-MCP).

The crystal is mounted at the bottom of a vertical liquid nitrogen cooled cryostat, which protrudes into the UHV chamber through an x, y, z, θ manipulator. The crystal temperature is controlled between 89 and 1300 K using liquid nitrogen cooling and radiative heating or electron bombardment from a tungsten filament located being the crystal. The crystal is cut and polished to expose a curvature encompassing ~ 31 ° along the $[11\bar{2}]$ direction with the (111) surface at the apex. Figure 5.1a shows our laboratory coordinates for the crystal. The z axis runs along the vertical direction and the x axis runs along the horizontal direction. The supersonic molecular beam and the electron beam of the LEED/AES optics are incident along the y axis. As figure 5.1b shows, the upper part of the crystal consists of (111) terraces with B-type steps. The lower part of the crystal contains A-type steps. By moving the crystal along the z axis, we can change the surface exposed to our molecular beam and LEED/ AES optics from beyond Pt(553) (z=+3.19 mm, α=+12.3 °) to Pt(533) (z=-3.74 mm, α=-14.4°) smoothly. Here, α is the angle between the surface normal at the indicated z position and [111].

The crystal is cleaned by sputtering at 0.5 keV with $\sim 2.0\mu A$ Ar^+ current ($p_{Ar} = 6.0 \times 10^{-6}$ mbar) for 5 minutes at surface temperature

900 K. This is followed by an oxidation at the same surface temperature (3 minutes, $p_{O_2} = 3.5 \times 10^{-8}$ mbar) and annealing at 1200 K for 3 minutes. This cleaning procedure is repeated 3-5 times before the last clean cycle. For the last cycle, we only sputter and anneal. Two different annealing temperature are used, 850 K and 1200 K, respectively.

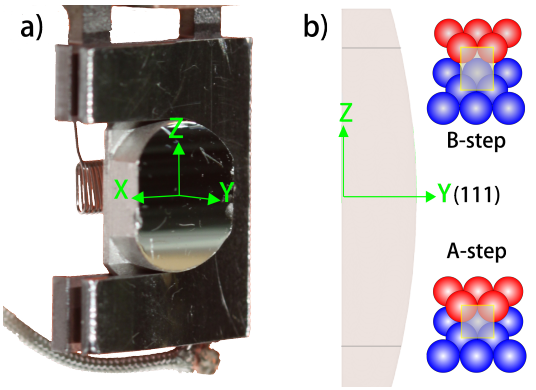

Figure 5.1: Schematic of the crystal. The crystal is mounted onto the 'U' shape sample holder. The x and z axes are along horizontal and vertical direction, respectively. The molecular beam and LEED/AES optics are incident along the y axis. Figure b) is a schematic view along the x axis. The upper part of the crystal contains B-type steps and the lower part of the crystal contains A-type steps.

The molecular beam is generated by expansion of a gas mixture at a total pressure of $\sim$ 2.0 bar through a tungsten nozzle with a 28 μm diameter orifice. The beam is shaped by two skimmers (subsequent diameters from the expansion nozzle are 0.45 mm and 2.5 mm). Two flags, one positioned in the second differential pumping chamber and one in the UHV chamber, and a chopper wheel located in the first differential chamber, modulate the beam. The two flags are used to determine the absolute dissociation probability using the King and Wells (KW) technique[10]. The chopper wheel is a fast rotating disk ($\sim$250 Hz) with two broad (17 mm) and two narrow (0.85 mm) slits. It is used to determine the kinetic energy and the energy distribution using time-of-flight (TOF) techniques.

A home-made gate valve separates the second differential pumping chamber and the UHV chamber. It consists of a rectangular plate with four orifices. It slides through a groove cut into a solid flange with knife edges on both sides. A linear feedthrough accurately positions the sliding plate within the groove. The sliding plate contains, besides an O-ring to seal the UHV chamber, one larger hole with a diameter

of 6.2 mm, one medium-sized hole with diameter of 3.2 mm, one small hole with diameter of 1.6 mm, and a rectangular slit of 3.2 mm in horizontal direction and 0.065 mm in vertical direction. By choosing different orifices on the plate, we can change the molecular beam's size and shape at the crystal position inside the UHV chamber.

For HD formation experiments, we use a mixture of H_2 (6N, Linde Gas, Rotterdam, The Netherlands), D_2 (2N8 isotopic purity, Linde Gas, Rotterdam, The Netherlands) and Ar (5N7, Air Products) to generate the supersonic beam. The beam is expanded at room temperature. The most probable energies of H_2 and D_2 are 10.9 meV and 22.7 meV, respectively, as determined by TOF techniques. The surface temperature of the crystal is 530 K. At this temperature, H_2, D_2, and HD desorb instantaneously. HD formation is measured using the King and Wells (KW) technique. However, while the reactant intensity drops when the beam is allowed to impinge upon the surface, the HD partial pressure detected by our QMA increases when the $H_2/D_2/Ar$ beam hits the surface. Figure 5.2 shows a series of measurement of HD formation when moving the crystal along the z axis. In this example, we probe reactivity change across the curved surface at 15 locations, each separated by 0.5 mm. In between moving the crystal from one to the next location, the beam is blocked by moving both beam flags sequentially. The simultaneously detected H_2 and D_2 signals are also shown. The signals clearly show the opening and closing of both flags. When we open the first flag in the second differential pumping chamber, the beam enters into the UHV chamber. The H_2 and D_2 signals clearly increase. The HD signal also increases, even though the beam does not impinge directly onto the crystal. This increase is due to HD contamination in the molecular beam, presumably from H-D exchange in the nozzle, and/or from the effusive load onto H-D reactive surfaces in our chamber (e.g. the hot tungsten filament behind the Pt sample and the Pt sample itself). When we open the second flag located in the UHV chamber, the beam impinges directly onto a narrow part of the Pt crystal. The H_2 and D_2 signals drop but the HD signal increases further. When we close the second flag but keep the first flag open, the H_2 and D_2 signals increase and the HD signal drops to its earlier level. When both flags are closed, all the signals drop to their residual values. All three signals change simultaneously. The green vertical line with arrow heads in figure 5.2 indicates how we quantify in a relative sense the HD formation by each separate part of the crystal when the

beam directly impinges onto it. We use the QMA intensity difference observed when opening and closing the second flag. Compared to H_2 and D_2, the HD signal has a high signal-to-noise ratio, especially when the reactivity is low. The lower background signal for HD allows an increased channeltron voltage for HD detection in comparison to H_2 and D_2, increasing our sensitivity to the surface reactivity as compared to detection of the removal of H_2 and D_2. Those signals are more noisy than the HD signal. In figure 5.2, the HD signal also clearly shows reactivity changes for different z positions. There is clearly HD being produced at the (111) apex (8th exposure), but HD production increases rapidly when moving onto either type of stepped surfaces.

A slightly complicating factor appears when scrutinizing the data in figure 5.2. The absolute QMS intensities for H_2 and D_2 seem to change each time we admit the beam to the chamber. The rise resulting from admitting the molecular beam to the UHV chamber increases only a little each time, but over the entire experiment quite substantially. This increase is not caused by an instability in our molecular beam. All pressure gauges in the differential stages and UHV chamber indicate that the beam is stable. The origin of the increasing QMS intensity for H_2 and D_2 lies in reduction of the channeltron's inner surface when using a reducing gas. It increases the channeltron's sensitivity, presumably by lowering the work function of the glass through reduction of its outermost layer. We have noticed this effect also in experiments performed with the same type of QMS on a different molecular beam-UHV apparatus (see Chapter 4) and the opposite in experiments using O_2 molecular beams and the same Baltzers QMA200 in the molecular beam apparatus used for the current study[109].

Normalizing the rise of H_2 and D_2 to the first admission of the beam to the UHV chamber, we obtain a functional form of the sensitivity change. It is shown in figure 5.3 for H_2 and D_2 as a function of the number of times that the beam was admitted to the UHV chamber. Here, we show data for a similar experiment as shown in figure 5.2, however, the change in z position was reduced and the beam was admitted 41 times to cover the entire curved surface range. The first admission is numbered as "0" and used for normalization. As beam admission is computer-controlled and uses a fixed time for each admission, the x axis is proportional to the integrated flux of reducing gases admitted to the chamber. For both isotopologues we see the same sensitivity change throughout the entire experiment. It is nearly

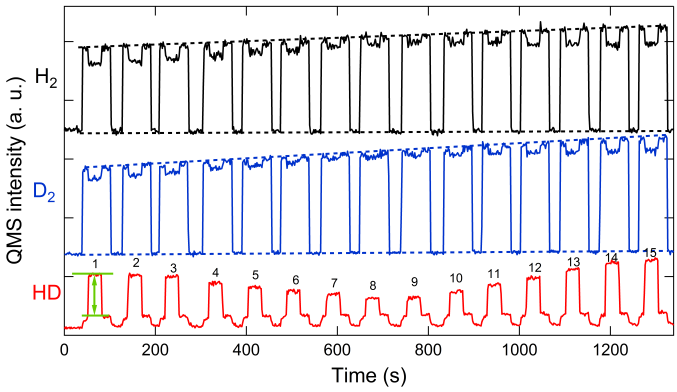

Figure 5.2: An example of a continuous measurement of HD formation by moving the crystal along z axis with a 0.5 mm step. The H_2 and D_2 signals are also showed simultaneously. The green lines indicate how we determine HD formation.

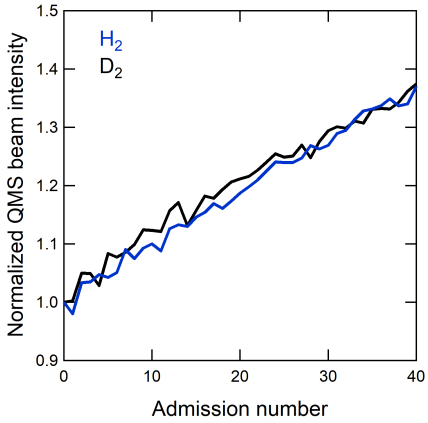

Figure 5.3: Normalized QMS signal intensities of H_2 (blue) and D_2 (black) versus number of times that the beam is admitted to the UHV chamber.

linear. Assuming that the sensitivity to HD follows the manner trend, we correct the HD pressure rise for impingement onto each separate part of the curved surface for this QMS sensitivity change in each run of measurements across the crystal. Obviously, for experiments that take longer as smaller steps in z position are used, the effect is larger.

5.3 Results

5.3.1 The molecular beam size at the surface

As the HD formation is sensitive to step density and step density varies vertically along the crystal's surface, using a circular or rectangular shaped beam influences the measured HD production. To measure the exact size of our beam, we move the crystal horizontally across the beam and measure the intensity of HD (m/e=3) using the QMA200 mass spectrometer. Figure 5.4a shows the results of these measurements when the beam is shaped using the 1.6 mm diameter circular orifice in the sliding beam valve. The blue circles are the HD intensity at different x positions. HD production is nearly identical at -2.0 mm and +2.0 mm. Beyond these positions, it drops (nearly) linearly with position. From the known width of the crystal, ie. 7.0 mm, and the 4.0 mm wide plateau we calculate the beam size at the crystal position. It is ϕ 3.0 mm. The solid line in figure 5.4a is a simulation of the overlapping area of a ϕ 3.0 mm circle moving along the x axis on the 7.0 mm wide crystal surface. The simulation agrees well with our measurement. Figure 5.4b shows the result of the same experiment using the 3.2×0.065 mm slit as our molecular beam shape-defining orifice. The red circles are the measured HD intensity from our QMA versus x position. As the inserted diagram shows, we now have a much more limited range to move the crystal to keeping the HD intensity identical. The solid red line in figure 5.4b is a simulation of the overlapping area of the 6.0 mm wide rectangle with the crystal along the x axis. The simulation again agrees very well with our measurement. The beam's size at the crystal changes by a factor of $\sim$1.9 when varying between these two shape-defining orifices. The vertical size of the beam at the crystal can thus be calculated independently for the 3.2×0.065 mm slit orifice. It is $\sim$0.12 mm. The red horizontal bar in the inserted picture of figure 5.4b shows the size of the beam in comparison to the crystal. As shown in the inset by the dashed rectangle, the rectangular beam's size limits the extent over which we can probe reactivity across the surface without more complex deconvolutions. The range of z positions is limited to $\pm$2.65 mm from the apex when using the slit orifice.

The points that are aberrant at the negative x side are caused by the 'U' shaped sample holder, shown in figure 5.1a. At the negative x

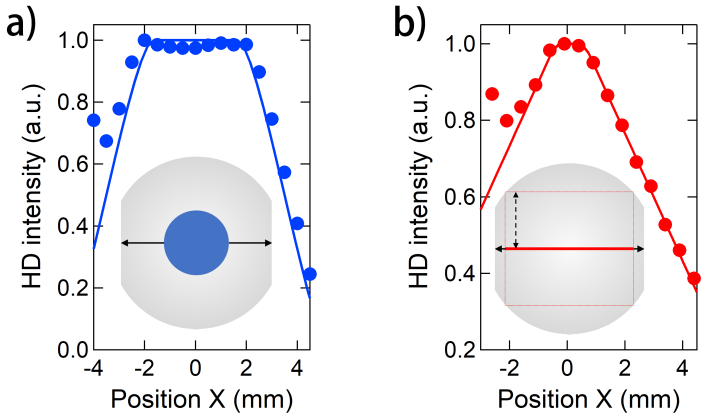

Figure 5.4: HD intensity variation with x-position in the laboratory frame as measured by the QMA200 upon exposure to a H_2/D_2/Ar beam for a) a 1.6 mm diameter circular orifice and b) a 3.2×0.065 mm wide rectangular orifice. Inserted schematics show the molecular beam size in comparison to the crystal. Blue and red circles in figures a) and b) show the measurements. The solid line in a) is a simulation of the convoluting beam and crystal areas for moving the crystal along the x axis assuming a 3.0 mm diameter beam. The solid line in figure b) shows the same simulation using a 6.0 mm wide rectangle. The red bar in the insert of b) shows the extracted 6.0× 0.12 mm molecular beam size at the crystal position in comparison to the crystal's surface. The dashed rectangle indicates the usable area for the 6.0 mm wide beam. The crystal can only be moved along z axis ±2.65 mm from the center when using the slit orifice without the beam impinging onto the crystal holder.

side, the beam impinges onto the sample holder, which is coated with a thin Pt foil. The polycrystalline foil is reactive and HD molecules are generated, causing the higher than expected HD intensity. At the positive x side, the sample holder is open. The part of the beam not impinging onto the same does not strike a reactive surface and does not contribute to the H-D exchange reaction.

5.3.2 HD formation along z axis

Figure 5.5a shows how the local angle between the surface normal and [111], α, (black circles) and the ideal monoatomic step density (red squares) change with the z position of our crystal. To reach $\alpha = -14.4°$, we require $z = -3.74$ mm at the A step side. This position responds to the Pt(533) surface, i.e. Pt[4(111)×(100)]. Moving to the opposite side, we find at 12.3°, i.e $z = +3.19$ mm at the B-type

step side, Pt(553), i.e. Pt[4(111)×(110)]. The step density changes linearly with the distance from the center of the crystal. The slopes of step density with z are identical for both sides of the center. However, reaching the same terrace width, e.g. $n = 4$ for the A and B-type steps, is not the same as the step is structured differently.

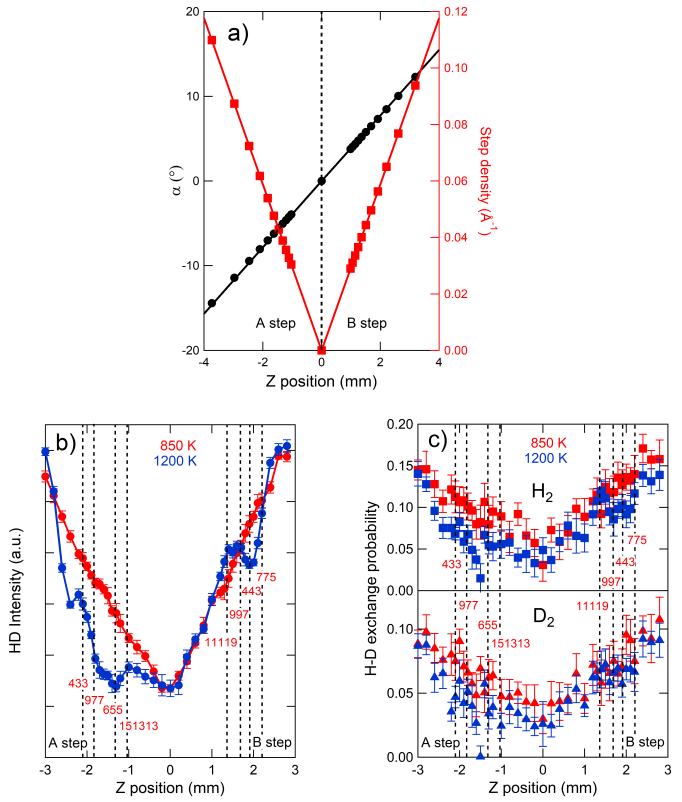

Figure 5.5: a) shows the angle α (black circles) and the step density (red squares) versus the z position on the crystal. b) shows HD formation after the crystal is cleaned using an identical procedure but annealed at different temperature as a final step. The crystal is moved along the z axis with x fixed at 0.0 mm. The data color-coded with red and blue represent the final anneal temperature of T_{anneal} =850 K and 1200 K, respectively. The dashed lines indicate non-reconstructed surface structures. c) shows in the upper panel the absolute H-D exchange probability for H_2 and in the lower panel for D_2 for the same final annealing steps as used in b). The definition of H-D exchange probability is provided in the text.

Figure 5.5b shows the HD formation from the impinging H_2/D_2/Ar beam shaped by our rectangular orifice when moving the crystal along the z axis. The x position is fixed at 0.0 mm. The data presented

with red markers are obtained after the crystal is annealed in the final cleaning cycle at T_{anneal} = 850 K. HD production is, to a first approximation, linear from the center of the crystal to both sides over the entire range. As the dissociation of H_2 and D_2 depends linearly on the availability of steps at these conditions [29, 101], it suggests that the step density of the crystal increases linearly from the center to both A and B step sides.

The data indicated with blue markers in figure 5.5b are obtained when the crystal is cleaned by the same cleaning procedure but finally annealed at T_{anneal} = 1200 K. HD formation is clearly not linear with position over the entire range on both sides. On the A-type step side, the HD intensity is lowered at all positions in comparison to data obtained after annealing at 850 K and only recovers to approximately the same value at −3.0 mm, i.e. where our beam partly impinges onto the crystal holder. The reactivity increases linearly from 0.0 mm to −1.0 mm with a reduced slope. Then it drops from −1.0 mm to −1.3 mm. It subsequently rises again with a slope that is steeper than observed in the data obtained for T_{anneal} = 850 K. A second dip in the nearly linear increase in overall reactivity occurs just beyond -2.0 mm.

On the B-type step side of the apex in figure 5.5b, the HD intensity initially increases linearly from 0.0 mm to +1.4 mm with an identical slope as found for the data obtained at T_{anneal} = 850 K. Then it sharply drops from +1.4 mm to +1.9 mm. Subsequently, it rises again with a steeper slope as found for the 850 K data. At the z position of +1.9 mm the HD intensity for T_{anneal}= 1200 K are approximately identical to the values obtained for T_{anneal} = 850 K. The dependence of local reactivity on the annealing temperature in the final cleaning cycle indicates surface structural differences induced by the final annealing step.

In figure 5.5c, upper panel, we report for the H_2 isotoplogue the absolute H-D exchange probability as a function of z position. This probability equals the drop in the H_2 QMS intensity when opening the second flag divided by the rise in H_2 QMS intensity when admitting the beam (i.e. opening the first flag). The latter is proportional to the number of H_2 molecules in the beam entering the chamber. The former is proportional to the number of H_2 molecules dissociating and not returning as H_2 to gas phase, but as HD. Clearly, for each H_2 molecule that dissociates and is involved in H-D exchange, two HD molecules are produced and detected at m/e = 3. We use the same color coding

as in 5.5b to indicate T_{anneal} as 850 K (red) and 1200 K (blue). The bottom panel shows the same information for D_2. Clearly, the general trends observed for HD production in figure 5.5b are reproduced. The chance for both H_2 and D_2 to dissociate and recombine with an atom of the other isotopic kind increases with step density. It also decreases for $T_{anneal} = 1200$ K on extensive parts of the A-type step side of the curved surface, in particular near Pt(655), although the position of largest dip differs by ~ 0.1 mm. On the B-type step side, the data show a dip in H-D exchange probability near Pt(443). Clearly, the signal-to-noise level is considerably worse in these panels than in figure 5.5b. It is noteworthy that the absolute H-D exchange probabilities are not identical for H_2 and D_2 at the same surface positions. They differ by approximately a factor of 1.5.

5.3.3 LEED analysis of the surface structure

To study local changes of the crystal surface by diffraction, we minimize the electron beam size of our LEED optics. A micro-channel plate (MCP) LEED should allow for the use of a smaller electron beam diameter than conventional LEED optics. Our electron beam diamater is estimated to be 0.3 mm, based on a measurement of current to the crystal from the electron beam when translating the crystal parallel to the face of the optics. However, the design of MCP-based LEED/AES optics distorts the observed LEED pattern. The MCP plate is flat while proper visualization of the Ewald sphere requires a hemispherical screen. We have previously discussed how the distorted pattern can be corrected [13] and have written a software program to modify photographic images taken of the LEED pattern and correct the distortion.

Figure 5.6a shows three examples of corrected photographic images of LEED patterns taken at z=-2.2 mm, z=0 mm and z=+2.2 mm. In this figure, vertical spot splitting is clearly observed for the two images not taken at the apex. The vertical splitting indicates that the steps lie in in the x-y plane in the laboratory frame. To analyze the dependence of spot-splitting in the LEED pattern on the z position of the crystal, we select a slice of the $(0, -1)$ LEED spot be cropping the image to 4×200 pixels. An example is shown in figure 5.6b. We subsequently connect a series of such slices for different z positions. Figure 5.6 c and d show the result. The crystal was moved along z axis with a

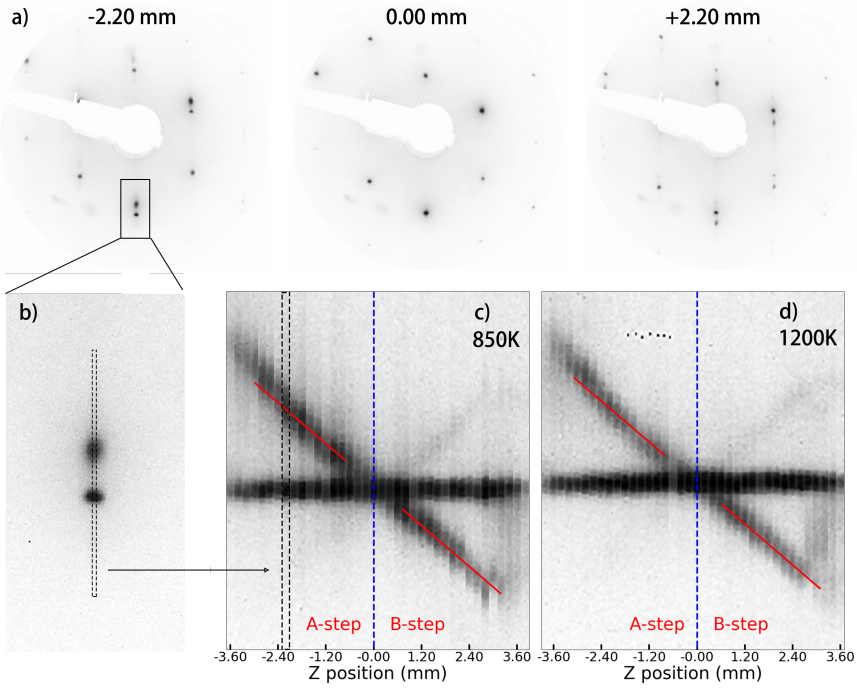

Figure 5.6: Figure a) shows the photographic images of LEED patterns taken at z=-2.2 mm, z=0 mm and z=+2.2 mm after the crystal is annealed at 850 K. Figure b) shows the expansion of the solid rectangle in figure a). The dash rectangle shows the slice we used to cut the center of $(0, -1)$ LEED split-spot (4×200 pixels). Figure c) and d) show a connected series of such slices at different z positions after the crystal is annealed at 850 K and 1200 K, respectively. The red lines are the theoretically predicted values of spot-splitting for different stepped surfaces[110].

0.2 mm step to obtain these images. Figure 5.6c visualizes the spot splitting versus z positions after annealing at 850 K. The spot splitting increases (roughly) linearly from the center to both A-type and B-type step sides. At the edge of the A-type step side, spot splitting diverges from the linear behavior observed closer to the apex. Spot-splitting increases there. The red lines drawn in the image represent the calculated spot-splitting for monoatomically stepped Pt(111) surfaces[110]. Our experimental data agree over a large extent very well with the calculated values, with only a minor deviation occurring beyond -2.5 mm, i.e. near the edge of the crystal. Figure 5.6d shows the same spot-splitting versus z position after annealing to 1200 K as well as the theoretical values. At first glance, differences between figures 5.6c and 5.6d seem small and spot-splitting after 1200 K again agrees well

with the theoretically predicted values for mono-atomic steps. However, differences appear when studying the images in more detail. For example, while in figures 5.6c and 5.6d, the horizontal branch created by connecting the slices of images shows a nearly fixed width (i.e. spot diameter) and intensity (i.e. shade of grey), the branches at $-45°$ (i.e. rotated clockwise) created by the second LEED spot is less intense for T_{anneal} = 1200 K, particularly at some z positions.

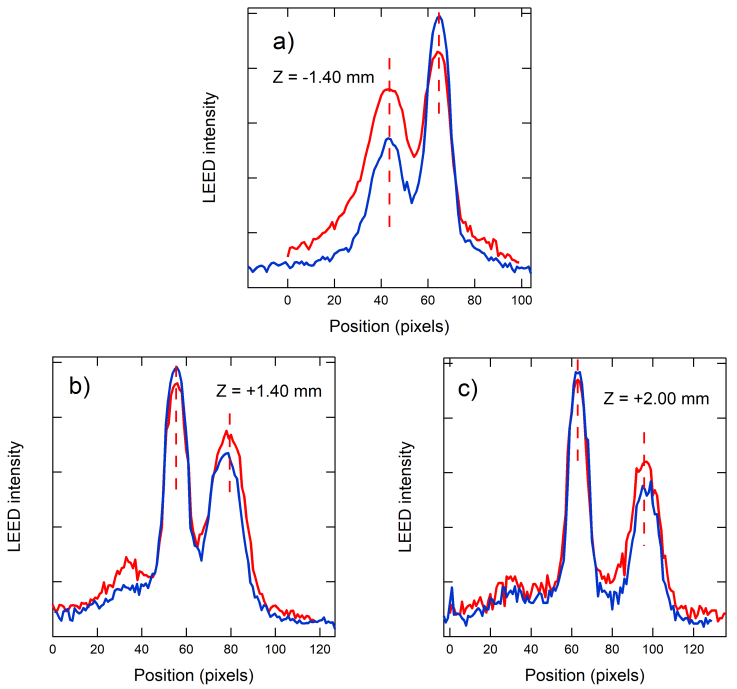

Figure 5.7: LEED intensity profiles of the split $(0, -1)$ spot at different z positions of the crystal. The red and blue curves indicate the two different annealing temperatures, i.e. 850 K and 1200 K, respectively. The red dashed lines indicate the peaks' positions of the red curves as comparison for the blue curves.

On the A-type step side, figure 5.5b shows a strongly reduced HD productivity at z=-1.32 mm for T_{anneal} = 1200 K (blue data). This position corresponds to the unreconstructed (655) or Pt[11(111)×(100)] surface. The HD productivity drops nearly to the level of the crystal's apex. Figure 5.7a shows the intensity of the (0 -1) split spots from the LEED patterns at z=-1.40 mm for annealing at both annealing temperatures (red for 850 K, blue for 1200 K). The peaks' positions are identical for both treatments, but the intensity ratio of the peaks has

clearly changed. The higher annealing temperature (blue line) yields a reduced intensity for the left peak (upper spots in figures 5.6c and 5.6d) and an increased intensity for the right peak (lower spot in figure 5.6d).

On the B-type step side, the HD productivity seems increased slightly by annealing at 1200 K instead of 850 K for $z = +1.36$ mm. This position corresponds to the (11 11 9) or [10(111)×(110)] surface. It is followed by reduced reactivity at $z = +1.91$ mm, i.e. nominally the (443) or [7(111)×(110)] surface. Figure 5.7b and c show the LEED intensity profiles for the (0 -1) spots at $z = +1.40$ mm and $z = +2.00$ mm, respectively. Here, the left peak corresponds to the spot causing the horizontal branch in figure 5.6c and 5.6d. For both z positions, the LEED intensity profiles do not differ much. Upon detailed inspection, in figure 5.7b, the peak on the right side shifts a little to the left after annealing to 1200 K (blue line) compared to the T_{anneal} =850 K case (red). For figure 5.7c, the opposite occurs.

5.4 Discussion

When annealed at 850 K, both HD formation in figure 5.5b and LEED spot splitting in figure 5.6c suggest a linear relation between step density and distance from the crystal's apex. This occurs at both sides of the apex. The experimentally determined LEED spot splitting is quantitatively in agreement with calculated values for monoatomic steps. Spot splitting is also mostly identical on both sides of the apex. The only clear difference between the A and B-type step sides of the crystal is a third diffraction spot weakly visible on the B-type step side. It causes the faint +45° branch in figure 5.6c and is also observed in the intensity plot in figures 5.7b and 5.7c as a small third diffraction feature equidistant to the center peak. Such triplets in LEED patterns may occur when the inherent LEED intensity variation from constructive interference caused by the terraces captures three 'rods' of interference caused by the step array[12]. It is surely not caused by step doubling or faceting as that would lead to a triplet with the third spot appearing in between the original two spots as, e.g., observed for restructuring of Pt(997) [106].

HD formation after T_{anneal} = 850 K is nearly identical on both sides of the crystal's apex. Figure 5.5b shows through a slightly steeper

slope on the B-type step side that HD formation increases more rapidly with step density than for A-type steps. This result may be expected as B-type steps also show higher initial dissociation probabilities than A-type steps in the incident energy regime where dissociation is dominated by steps [101]. Hence, the linear HD formation with position and the non-zero reactivity at the apex in figure 5.5b indicate that HD is being produced by (111) terraces with additional aid of steps, whose density increases linearly with the distance to the apex. The aid of the steps in increasing HD formation may be expected to lie predominantly in the dissociation of H_2 and D_2, and not so much in increasing desorption rates.

We noted that the absolute H-D exchange probabilities for H_2 and D_2 from figure 5.5c were not identical. A comparison of the absolute H-D exchange probabilities reported on the y axes in the upper and lower panels shows that the fraction of H_2 to return as HD is higher than for D_2 molecules. The ratio is approximately 1.5. We consider the reaction kinetics to trace its origin. First, we define the rates of elementary steps. The dissociation rates, R, for H_2 and D_2 are defined by their incident fluxes, Φ_{H_2} and Φ_{D_2}, and dissociation probabilities, S_{H_2} and S_{D_2}.

$$R_{diss,H_2} = \Phi_{H_2} \cdot S_{H_2} \tag{5.5}$$

$$R_{diss,D_2} = \Phi_{D_2} \cdot S_{D_2} \tag{5.6}$$

The part of the impinging flux scattering without dissociating is given by the remainders, $\Phi_{H_2} \cdot (1\text{-}S_{H_2})$ and $\Phi_{D_2} \cdot (1\text{-}S_{D_2})$. Also, we may safely assume steady state conditions. It is most prominently observed in figure 5.2 in the flat HD intensity profile when the beam impinges onto the crystal. In a steady state, the surface coverage of H_{ads} and D_{ads} (Θ_H and Θ_D) do not change as a function of time. This requires that rates of change due to dissociation equal rates of change due to desorption for Θ_H and Θ_D independently. Desorption occurs in part as the original species, i.e. H_2 and D_2, and in part as HD. Therefore,

$$2 \cdot \Phi_{H_2} \cdot S_{H_2} = 2 \cdot k_d \cdot \Theta_H^2 + k_d \cdot \Theta_H \cdot \Theta_D \tag{5.7}$$

and

$$2 \cdot \Phi_{D_2} \cdot S_{D_2} = 2 \cdot k_d \cdot \Theta_D^2 + k_d \cdot \Theta_H \cdot \Theta_D \tag{5.8}$$

where k_d is the isotopologue-independent rate constant for desorption. Figure 5.8 illustrates this graphically, with colored areas indicating directly scatter flux (blue) and flux that dissociated but returned as the original isotope (red). The sum of these components do not result in a drop of the partial pressure while the beam impinges onto the sample. Their relative contributions cannot be distinguished. As our definitions of the H-D exchange probabilities for H_2 and D_2 (EPH_2 and EPD_2) are given by

$$EPH_2 = \frac{k_d \cdot \Theta_H \cdot \Theta_D}{2 \cdot \Phi_{H_2}} \tag{5.9}$$

and

$$EPD_2 = \frac{k_d \cdot \Theta_H \cdot \Theta_D}{2 \cdot \Phi_{D_2}}, \tag{5.10}$$

the observation that $EPH_2 > EPD_2$ by a factor of ∼1.5 requires that $\Phi_{D_2} \approx 1.5 \times \Phi_{H_2}$. This compares well with the ratio of flow rates used to create the three-component supersonic molecular beam (4 ml/min D_2, 2.9 ml/min H_2, and 1 ml/min Ar). Mass focusing in the molecular beam or differences in the calibration of the flow controllers may cause the remainder of the difference. Noteworthy, its higher incident kinetic energy lowers the dissociation probability in this regime for D_2 [26, 28–31].

When annealed at 1200 K, reactivity toward HD formation in figure 5.5 changes on both sides of the crystal. For the A-type step side, it is reduced over the entire range and only recovers when our molecular beam overlaps with the edge of the crystal. It actually becomes slightly more reactivity there, presumably because the higher annealing temperature allows cleans the sample holder better. The general reduction on this side of the crystal's apex is largest at Pt(655) or Pt[11(111)×(100)]. On the B-type step side, reduction in HD productivity is much more localized and centered at Pt(443) or Pt[7(111)×(110)]. From the linear relation between reactivity and step density observed for $T_{anneal} = 850$ K, results for 1200 K suggest dramatic surface structure changes that lower step densities on both A and B-type step sides.

The vicinal surface structure is determined by the balance between the step creation energy, the step-step repulsion energy, and the terrace energy [111]. A structure may become unstable if a physical variable (e.g. temperature) or chemical change (e.g. an im-

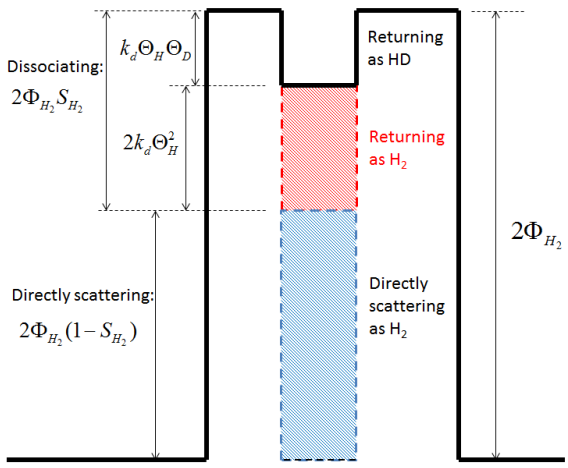

Figure 5.8: Graphical illustration of the relation between the measured partial pressures as the QMS intensity and the fluxes of H atoms impinging onto the sample and returning to the gas phase assuming instantaneous steady state conditions when opening and closing beam flags. While illustrated for H2, the identical picture holds for D_2 varying only by a different QMS sensitivity factor.

purity) causes changes to these energies. Several platinum surfaces are known to reconstruct. For example, step-doubling, which causes terraces to become twice as wide, has been reported by Somorjai and coworkers in a LEED study of Pt(997) being annealed in an O_2 atmosphere[112]. Comsa et al. also observed partial faceting and step-doubling of Pt(997) by high temperature annealing in oxygen using He atom diffraction and LEED[106, 107]. Hahn et al. also studied this system using He atom diffraction and scanning tunneling micrscopy (STM)[108]. First, they annealed the crystal in an oxygen atmosphere (1×10^{-7} mbar) at 700 K for several minutes and observed a partial step-doubling. Step-doubling was argued to be caused by modification of the step energy. On the clean surface, a double-height step costs more energy to create than two single monoatomic steps. If the interaction between the steps with attached O_{ads} lowers the energy cost for generation of double steps, step-doubling may appear. Second, they annealed the crystal at different temperature and observed thermal faceting on Pt(997). They demonstrated that thermal faceting is related to temperature-induced stress relief of the (111) terraces via reconstruction. Faceting is reversible. Annealing at 900 K for several minutes restored the nominal surface.

At any position along the curved surface, there will be a terrace

width distribution, similar or identical to those found on flat vicinal surfaces. The average terrace width is represented in LEED patterns by the spot-splitting to row-spacing ratio. With a curved Pt(111) single crystal very similar to ours, Walter et al. recently investigated the relation between the local surface structure and terrace width distribution using, a.o. scanning tunning microscopy (STM) and LEED[104]. They found linear relations over two regimes. For narrower terraces, step-step repulsion dominates and keeps distributions rather narrow. The ratio of the standard deviation, σ, to the average terrace width, $\overline{d}$, was found to be ~ 0.2. For wider terraces, entropy causes additional broadening of the distribution. It only sets in for (111) terraces of n $\sim$ 18 atom rows.

Our results in figure 5.5b, suggest that Pt(443) is more unstable at higher annealing temperatures than Pt(997). HD productivity reaches a local minimum at (443), whereas at (997) it is not much different from the data obtain for $T_{anneal} = 850$ K. We attribute it to a maximum in local restructuring, that reduces step density, hence the aiding effect of steps in dissociating impinging H_2 and D_2. If facets replace monoatomic steps, they are most likely of the $(11\overline{1})$ type, not of (110). Impinging reactants hit this facet at an angle of $\sim$70° from its surface normal. Luntz et al.[22] and we (see Chapter 3) showed that direct dissociative adsorption is hardly expected for this incident angle onto Pt(111) at the incident energies used here. Compared to the linear increase with step density for the 850 K case at Pt(443), the step-induced enhanced HD productivity (hence, the difference with the reactivity at the apex) drops by $\sim$ 33%. This requires that two-thirds of the monoatomic steps doubled, approximately one-half of the monoatomic steps tripled or a smaller fraction yielded larger facets. Interestingly, our LEED images taken nearest the (443) position in figure 5.6 and the intensity plots of the split spots in 5.7c show little difference. We believe this observation supports that only a small fraction of the surface has drastically changed, hence supporting the idea that larger $(11\overline{1})$ facets are formed rather than step doubling or tripling.

The absence of a significant change in HD reactivity resulting from the higher annealing temperature at the (997) location and the lack of significant differences in LEED patterns (figure 5.6 and 5.7) is also of interest. It shows that restructuring is very delicately dependent on terrace width. Whereas faceting appeared in studies of the nominal Pt(997) surface with its average 8-atom wide terraces[106–108], the

lack of an HD productivity drop argues against a significant loss of step density by faceting. From our experiments, it is clearly the 7-atom wide terrace that is the (most) unstable one in this vicinity. We believe that the previous ideas regarding restructuring of Pt(997) is actually a consequence of the 7-atom wide terraces occurring within the natural terrace width distribution present at the nominal flat Pt(997) surfaces studies by others. Walter et al. showed that the terrace width distribution increases linearly in this regime as a consequence of elastic interactions between steps[104]. For a terrace width of $n = 8$, a significant fraction of the distribution of terraces actually has slightly narrower terraces, e.g. $n = 7$. It seems likely that the observations of faceting on Pt(997) did not result from an instability of the 8-atom wide terraces, but from 7-atom wide terraces present on their samples. In this regard, it is of interest to reconsider whether a surface described by high Miller indices is actually well-represented using the Somorjai notation. The Miller index is derived from the macroscopic vector of the surface without specifying the local structure. It therefor does not imply a unique terrace width. The Somorjai notation describes the surface in terms of microfacets of a unique terrace width. At finite temperatures, the third law of thermodynamics requires entropy to deviate from unity. For a pure single crystal multiple microstates occur, which leads to the occurrence of a distribution of terrace widths.

On the A-type step side, changes in HD production after the higher temperature anneal cycle are much more drastic than on the B-type step side. At the (655) surface, reactivity is nearly identical to the (111) apex. Hence, step density must have been reduced so drastically that the additional reactivity provided by the few remaining steps only offsets the loss of active surface area from formation of (100) facets. The LEED diffraction patterns also show a clear loss in intensity near this position on the crystal in figure 5.7. Although spot-splitting does not change, hence the average step density not being altered, large amounts of faceting here results in a change in the intensity ratio of the split spots. We believe this is caused by narrowing of the sinusoidal intensity variation from (111) facets facing the LEED optics, while spot-splitting is not affected as the macroscopic angle does not change [12]. Hence, while the less intense spot suffers from narrowing of the (111) sinusoidal intensity variation, the more intense spot benefits. The lack of other spots appearing in LEED patters, suggests that there is no ordering to the (100) facets. The observation that the HD reactivity

is affected over a much broader ranges on the A-type step side of the apex than on the other side, suggests that (100) facet formation occurs much more readily than $(11\bar{1})$ facet formation. The step-step repulsion energy could be larger for A-type steps than for B-type steps, but the similarity of the step width distributions in the study by Walter et al. does not support this [104]. Stronger step-step interactions should cause a narrowing of the ratio of σ to $\bar{d}$. As the free energy of the 100 terraces is higher than that of 111 terraces, the different behaviors must be due to a step creation energy. Apparently, it is higher for the Pt A-type step than for the B-type step. Comsa et al. came to the same conclusion in an STM study of the shape of hexagonal pits in Pt(111) planes[113].

We come the conclusion that our chemical H-D exchange probe of surface structure competes very well with the physical probe of electron diffraction in studying reconstruction of stepped surfaces. Our MCP-LEED yields images from which we extract spot-splitting, agreeing very well with theoretical calculations of the ideal stepped surfaces. The vertical spot splitting indicates that steps lie horizontally on the surface. From qualitative interpretation of intensity plots we gather some information on potential surface structure changes, that are, however, much more easily observed in the H-D exchange when monitoring HD as a product. The same key points are present in the loss of H_2 and D_2, as represented by the H-D exchange probability, but signal-to-noise levels are much worse. The size of our molecular beam is also smaller than the electron beam from the LEED optics, leading to higher spatial resolution. In the absence of STM capability, the combination of LEED and the H-D molecular beam exchange probe allow us to study conditions leading to surface restructing and confirm which conditions lead to a linear relation between step density and distance to the apex for this Pt curved crystal.

On a final note, we return to the combined STM-photoemission study by Walter et al.[104]. They use repeated sputtering and annealing cycles to clean their surface, very similar to our methods. They anneal their crystal at 1073 K, whereas the Pt(997) surface is known to develop faceting at 980 K[106–108]. Our measurements confirm faceting in this regime using a higher annealing temperature, and suggest that it is probably Pt[7(111)×(110)] that restructures much more so than Pt[8(111)×(110)]. The absence of any comments on restructuring in this regime in Walter's paper is disturbing, especially since

they do comment on lack of evidence for macroscopic alterations in the curvature of the crystal.

5.5 Summary

At low incident kinetic energy, HD formation from a mixed H_2-D_2 molecular beam on a curved Pt surface is related to Pt step density. Using the appropriate cleaning procedure with a final anneal step of 850 K, a smooth step density gradient is represented by a linear increase in HD formation with distance from the crystal's (111) apex. A LEED study confirms the orientation of steps relative to the curvature of the crystal and suggests the same smooth variation in average terrace width. When annealed at 1200 K, HD formation is clearly reduced over the entire on A-type step side, most predominantly near (655), most likely resulting from (100) facet formation. On the B-step side, faceting occurs very locally at (443). LEED studies fail to show this ostentatiously. We only find indirect evidence of restructuring in intensity variations of split spots. Our H-D exchange probe is therefore much more sensitive to local restructuring than LEED. Noteworthy, the spatial resolution allows us to pinpoint positions where a delicate balance between step-step repulsion, surface and step energies, leads to restructuring more facile than experiments using flat single crystals studied using STM. It even allows us to correct the previously assumed restructuring of Pt[8(111)×(110)] from He atom diffraction, LEED and STM measurements on Pt(997) indicating that it is actually Pt[7(111) × (110)] that causes faceting. For reason of the (hkl) Miller indication for a real vicinal surface at finite temperature inherently requiring a distribution of stepped (or kinked) surfaces, rewriting it in the Somorjai notation, for example as [n(111) × (110)], is formally incorrect. A distribution cannot solely be described by its average.